ADVANCED FUNCTIONAL MATERIALS
www.afm-journal.de

An Ultrasensitive Perovskite Single-Model Plasmonic Strain Sensor Based on Piezoelectric Effect

*Meili Li, Junfeng Lu, Peng Wan, Mingming Jiang, Yepei Mo, and Caofeng Pan**

Interest in flexible photonics has been motivated by the development of artificial smart skins. In particular, coupling of photonics and mechanics can offer opportunities to realize ultrasensitive strain sensor, however, low-cost fabrication of flexible sensing device with desired photonic functionality remains a challenge. Hereby, the study reports an ultrasensitive strain-gauge sensor based on the poly(ethylenenaphthalate (PEN))/monocrystal Au/MgF_2/$CsPbBr_3$ nanorod/Al_2O_3/polyacrylonitrile (in short P/mAu/M/CPB@Al_2O_3@PAN), which are sensitive to nanoscale structure alterations of PEN substrate via the stress response of the single-mode laser based on the piezoelectric-effect. Wherein a low-threshold single-mode lasing (P_{th} ≈ 170 nJ cm^{-2}) is achieved through coating Al_2O_3 on the $CsPbBr_3$ nanorod, producing the higher quality factor (Q ≈ 1637) to guarantee a much higher sensitivity in sensing application. Reversible spectral regulating of ≈3 nm in single-mode-lasing wavelength, with a subnanometre scale resolution <0.4 nm and the wavelength sensitivity (S_λ) as high as 160 nm RIU^{-1}, is validated in response to applied strain ranging from −1.31% to 1.31%. This work not only represents essential progress in construction of ultrasensitive and cost-effective flexible photonic sensor, but also lays the foundation for the potential application in smart photonic skins.

1. Introduction

Technologies based on electronic components soft and stretchable have accelerated advancements of flexible electronics in robotic smart skin, wearable, and health monitoring.[1,2] As an analogy, taking advantage of the noncontact nature, high color-resolvability, and ultrasensitivity to external stimuli of photons as signal carriers, flexible photonics will become an ideal strategy to extend the capabilities of artificial smart skins.[3–12] As yet, various integration schemes for photonic elements including integrating laser cavities,[6–8] filters,[9] and on-chip pliable waveguides,[3,11] which can dynamic manipulation of the lasing emission and photonic band structure via input pressure/strain signals. Indeed, such flexible photonic devices have also really exhibited superiority performance in optical modulation or sensing. For example, stretchable photonic crystal laser sensors benefit from the spectrally narrow lasing signals and immunity to electromagnetic interference, exhibiting highly sensitive and accurate sensing to local structural changing.[8,13–16] However, the complicated fabrication procedures that render the high fabrication cost led to the practical applications of optical strain-gauge sensor remaining a great challenge.

Piezoelectric semiconductor nanomaterials, such as ZnO,[4,17] GaN,[18,19] and metal halide perovskite etc.,[20–22] which have superb mechanical properties and piezoelectric-effect, have been widely studied in the field of optical strain sensors so far.[6] Such strain-induced nonlinear response optical devices mainly include photoluminescence imaging,[26] light emitting diode (LED) and laser,[3–12] which are indispensable modules of optical strain sensors. Importantly, all-inorganic halide perovskite $CsPbBr_3$ not only possesses piezoelectric polarization effect but also with strong light-matter interaction,[20,23–25,27] holding great promise for lowering the cost-effective of flexible photonic sensors, however, has been very limitedly reported so far. As for a strain-sensor, the sensing mechanism can be concluded as the lasing-mode variation induced by piezoelectric polarization effect of $CsPbBr_3$, which had been confirmed in our previous work.[18,20,21] In general, origin of piezoelectric effect is associated with the distortion of coupled $PbBr_6$ octahedra and atomic displacement with each octahedron, which induces surface polarization of $CsPbBr_3$ crystal to change the refractive index.[25,28] Because of specific field distribution of the resonances, however, lasing-mode peaks are highly sensitive to the local deformation of resonant cavities and environmental variation, such as refractive index as well as temperature.[8,13–16,21,29] Particularly in surface plasmon resonance (SPR) sensor, small refractive index change on the chip surface could be achieving higher sensitivity, such as in chemical,

M. Li, Y. Mo, C. Pan
Beijing Institute of Nanoenergy and Nanosystems
Chinese Academy of Sciences
Beijing 100400, P. R. China
E-mail: pancaofeng@buaa.edu.cn
J. Lu, P. Wan, M. Jiang
College of Physics
Key Laboratory of Aerospace Information Materials and Physics (MIIT)
Nanjing University of Aeronautics and Astronautics
Nanjing 211106, P. R. China
C. Pan
Institute of Atomic Manufacturing
Beihang University
Beijing 100191, P. R. China

The ORCID identification number(s) for the author(s) of this article can be found under https://doi.org/10.1002/adfm.202403840

DOI: 10.1002/adfm.202403840

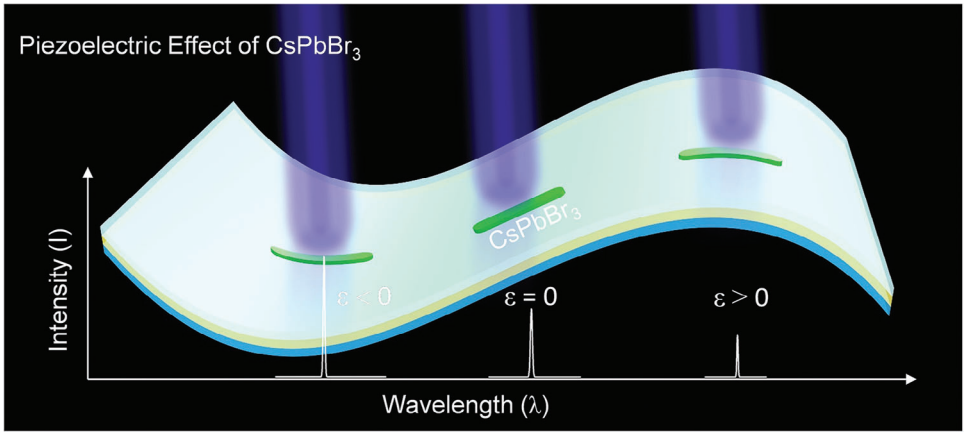

Figure 1. Schematic illustration of strain-gauge sensor based on piezoelectric effect. The outputting characteristic of $CsPbBr_3$ microcavity lasers is dependent on the piezoelectric polarization effect of $CsPbBr_3$ due to the substrate deformation. The strain-gauge sensor can distinguish diverse external forces according to the dynamically modulated lasing wavelength (λ) and intensity (I) under compressive strain ($\epsilon < 0$), tensile strain ($\epsilon > 0$) and without applied strain ($\epsilon = 0$).

pathogen detection, and food safety.[30–34] Therefore, fabrication of color-tunable and noncontact optical strain sensor based on the plasmonic cavity is essential to track micro- or nanoscale local deformation and to manipulate light-matter interaction.[7,8,13] Nevertheless, the sensitivity of an optical sensor is highly dependent on the structure and material of sensing element.[31] Plasmon sensor usually suffer from the intrinsically metal losses, increasing the line width of the resonance-curve and thus limiting their sensitivity.[30,31] Therefore, optimizing the quality factor (Q) of the cavity mode is essential to improve the sensitivity of a sensor.

In this work, we further designed the poly(ethylenenaphthalate (PEN))/monocrystal Au/MgF_2/$CsPbBr_3$ nanorod/Al_2O_3/polyacrylonitrile (in short P/mAu/M/CPB@Al_2O_3@PAN) device based on our previous work,[21] which allows for single-mode lasing, high stability (≈8 × 107 laser shots) and high-quality factor (Q ≈ 1637) with a remarkably low threshold (P_{th} ≈ 170 nJ cm^{-2}). Low-loss single-mode lasing dramatically increased the recognizability and accuracy of the sensing signals, which is ultrasensitive (S_λ ≈ 160 nm RIU^{-1}, strain $\epsilon \approx -1.31\%$) response to the local structural changes of the flexible substrate, good linearity of 0.986, and the spectral resolution as high as ≈600 ($\epsilon \approx -1.31\%$). Our strain-gauge sensors dynamically regulated the color-mapping to sense a mechanical signal via lasing wavelength and intensity, which is potential applications in color-perceived touching sensing.

2. Results and Discussion

Microcavity lasers as sensing information carriers can realize the high recognizable light signals due to the narrow emission linewidth (δ_λ).[6,8,18] Moreover, since the lasing output characteristics of piezoelectric semiconductor microcavity is sensitive to strain,[18,20,21] thus can transfer $CsPbBr_3$ nanorod onto PEN/mAu substrate to construct strain-gauge sensors (**Figure 1**). We further fabricated force-light coupling measurement system to investigate the corresponding relationship between lasing signals and mechanical strain (Figure S1, Supporting Information). When properly external mechanical stress applied along the growth direction of $CsPbBr_3$ nanorods, the effective refractive index (n_{eff}) of the microresonator changes due to the piezoelectric polarization effect, thus achieving the dynamical modulation of the lasing-mode and lasing putout intensity.[21] Therefore, such strain-gauge sensor can perceive the local deformation of the elastic substrate stimulated by the external force according to color and intensity mapping.[7,8,18]

The strain-gauge sensors (P/mAu/M/CPB@Al_2O_3@PAN) are fabricated by a simple method combing directional transfer and fixed encapsulation, of which used Al_2O_3 (thickness $T \approx 20$ nm) and PAN ($T \approx 30$ nm) serve as encapsulation layer (Figure S2, Supporting Information). Here, we first coated Al_2O_3 onto the $CsPbBr_3$ nanorods via atomic layer deposition (ALD), forming a dense Al_2O_3 film to protect $CsPbBr_3$ nanorods against oxygen and moisture in air,[26,35] and polar solvents[36] (Figure S3 and Note S1, Supporting Information). After being protected by ≈20 nm-thick Al_2O_3 layer, PAN as encapsulation layer can be well coated onto the surface of $CsPbBr_3$ nanorods@Al_2O_3 (in short CPB@Al_2O_3) to play a key role in fixing the $CsPbBr_3$ nanorods, thereby realizing the bend strain on the $CsPbBr_3$ nanorod by applying stress to PEN substrate.

In addition, another key role of Al_2O_3 in our strain-gauge sensor is the surface passivation effect to decrease nonradiative states.[26,37] Figure S4 (Supporting Information) presents the typical energy band diagram of $APbX_3$ perovskite material, where the trap states generally include shallow defects (surfaces) and deep defects (grain boundaries) that were identified as one of the main factors to induce the nonradiative recombination.[38,39] Shallow defects that are usually close to the band gap and with the lower formation energy, and are primarily X-site (Cl^-, Br^-, or I^-) vacancies[38,39] on the crystal surface, which generate a net positive charge due to under-coordinated metal Pb atom[40] (**Figure 2a**). However, surface species AlOH* generated in the process of ALD is of high reactivity active, it may provide passivation effect via contributed lone pair electrons to the center Pb atom or substitution of Br atoms to form a Pb-O coordinate bond with the perovskite surface which could increase the

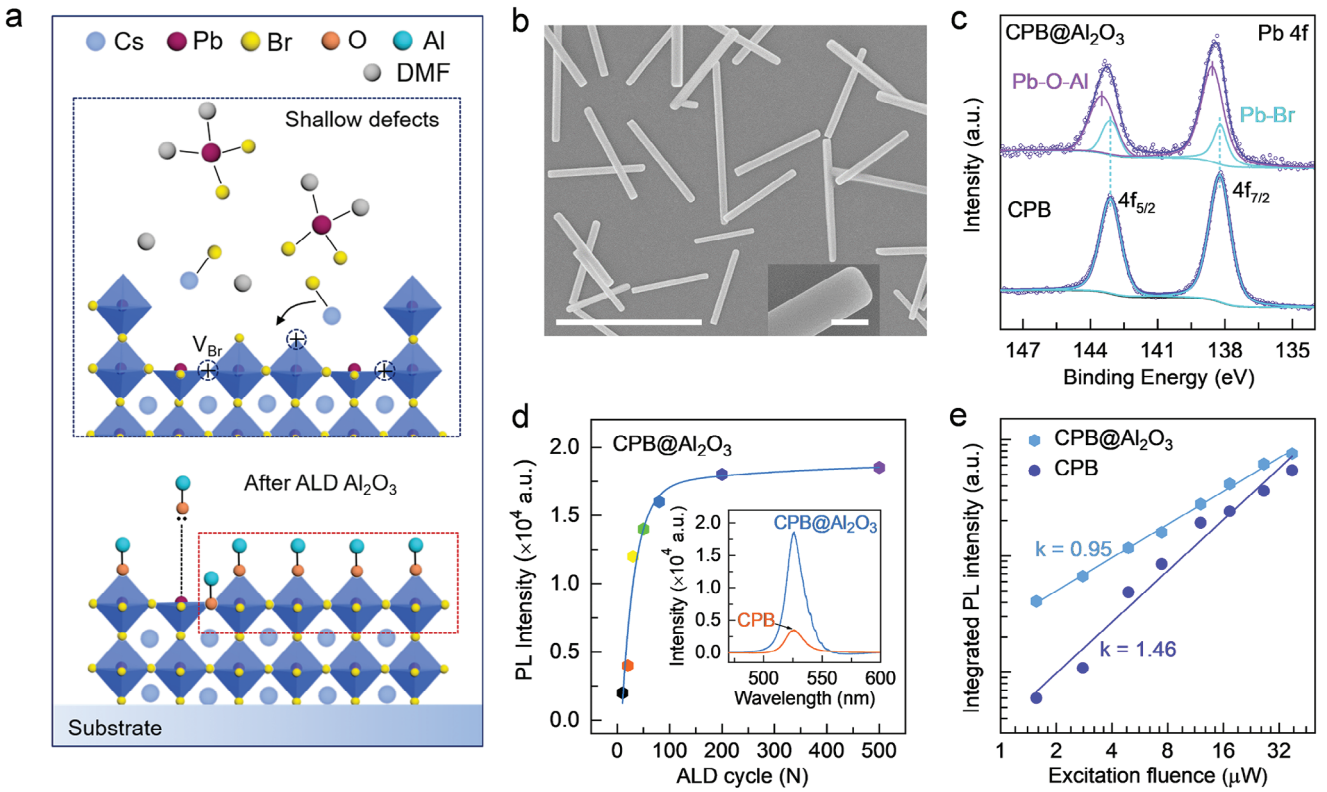

Figure 2. Structure and optical characterizations of $CsPbBr_3$ nanorods with Al_2O_3 modification. a) Schematic of the surface passivation mechanism of perovskite. b) SEM image of $CsPbBr_3$ nanorods with Al_2O_3 modification. Scale bar: 10 μm. Inset: magnified SEM image of one end of the $CsPbBr_3$ nanorod. Scale bar: 200 nm. c) XPS spectra of Pb 4f of the $CsPbBr_3$ nanorod with and without Al_2O_3 modification, demonstrating the formation of Pb–O–Al bonds. d) PL intensity of the $CsPbBr_3$ nanorod coated by Al_2O_3 with different ALD cycles. Inset: the corresponding PL spectra of the $CsPbBr_3$ nanorod with (≈200 ALD cycles) and without Al_2O_3 modification. e) Integrated PL intensities of the $CsPbBr_3$ nanorod with and without Al_2O_3 coating as a function of excitation powers.

radiative recombination rate[26,37,41] (Note S2, Supporting Information). Figure 2b shows the scanning electron microscopy (SEM) image of $CPB@Al_2O_3$ sample, which has the smoothed surface morphologies after Al_2O_3 modification. Here, these $CsPbBr_3$ nanorods range in length (L) from 7 to 9 μm, in width (W) from 200 to 300 nm, and thickness ≈130 nm. The corresponding element mapping images present uniform distribution of Cs, Pb, and Br elements with molar rations of 0.92: 0.85: 2.9 for the $CsPbBr_3$ nanorods after alumina coating, which conforms well to the $CsPbBr_3$ stoichiometry (Figure S5, Supporting Information). Besides, the Al and O elements were clearly uniform distributed on the $CsPbBr_3$ nanorods that indicate the formation of a dense Al_2O_3 film on that of the surface. X-ray diffraction (XRD) patterns show that the $CsPbBr_3$ nanorods and $CPB@Al_2O_3$ samples generate the identical diffraction peaks, which both can be indexed to the orthorhombic crystal phase of the $CsPbBr_3$ perovskite[42] (Figure S6, Supporting Information). Overall, these $CsPbBr_3$ nanorods modified by Al_2O_3 reserve their original morphologies, components, and crystal structures, which exclude the potential possibility to decrease $CsPbBr_3$ nanorods luminescence during the Al_2O_3 deposition.

We further conducted X-ray photoelectron spectroscopy (XPS) measurements to probe the chemical valence states of $CsPbBr_3$ nanorods before and after ALD coating (Figure S7a, Supporting Information). After 30 ALD cycles (≈3 nm-thickness Al_2O_3), O 1s new peak at 531.1 eV can be attributed to the Al-O bond which is the main driver for the efficient reactions of ALD[26,35,37] (Figure S7b, Supporting Information). Combined with Al 2p peak (74.46 eV) in the $CPB@Al_2O_3$ sample, it indicates that the Al_2O_3 has been successfully coated on the $CsPbBr_3$ nanorods[26,35,37] (Figure S7c, Supporting Information). Besides, the high-resolution scans peaks of Cs 3d, Pb 4f, and Br 3d clearly experience the movement toward high binding energy compared with bare $CsPbBr_3$ nanorods, indicating that the new chemical bond forms between the interface of $CsPbBr_3$ and Al_2O_3 (Figure 2c; Figure S7d,e, Supporting Information). While the Pb 4f peaks emerged at 143.1 and 138.2 eV (sky blue curve in Figure 2c) correspond to Pb $4f_{5/2}$ and Pb $4f_{7/2}$ levels in the Pb-Br octahedra, however, it slightly became broad and two additional high binding energy peaks were observed after Al_2O_3 modification.[26,37] The new peaks at 143.49 and 138.56 eV (purple curve in Figure 2c) can be attributable to the Pb–O–Al bonds, which may be due to the Al_2O_3 passivation of Pb atom on the $CsPbBr_3$ nanorods surface.[26] The generation of Pb–O–Al bonds is looking forward to reduce nonradiative transition and improve the quality factor of the cavity mode.

Figure 2d shows the photoluminescence (PL) spectra of $CPB@Al_2O_3$ samples with the number of ALD cycles. We observed the PL intensity of $CPB@Al_2O_3$ samples significantly enhanced up to 30 ALD cycles (≈3 nm-thickness Al_2O_3) and then

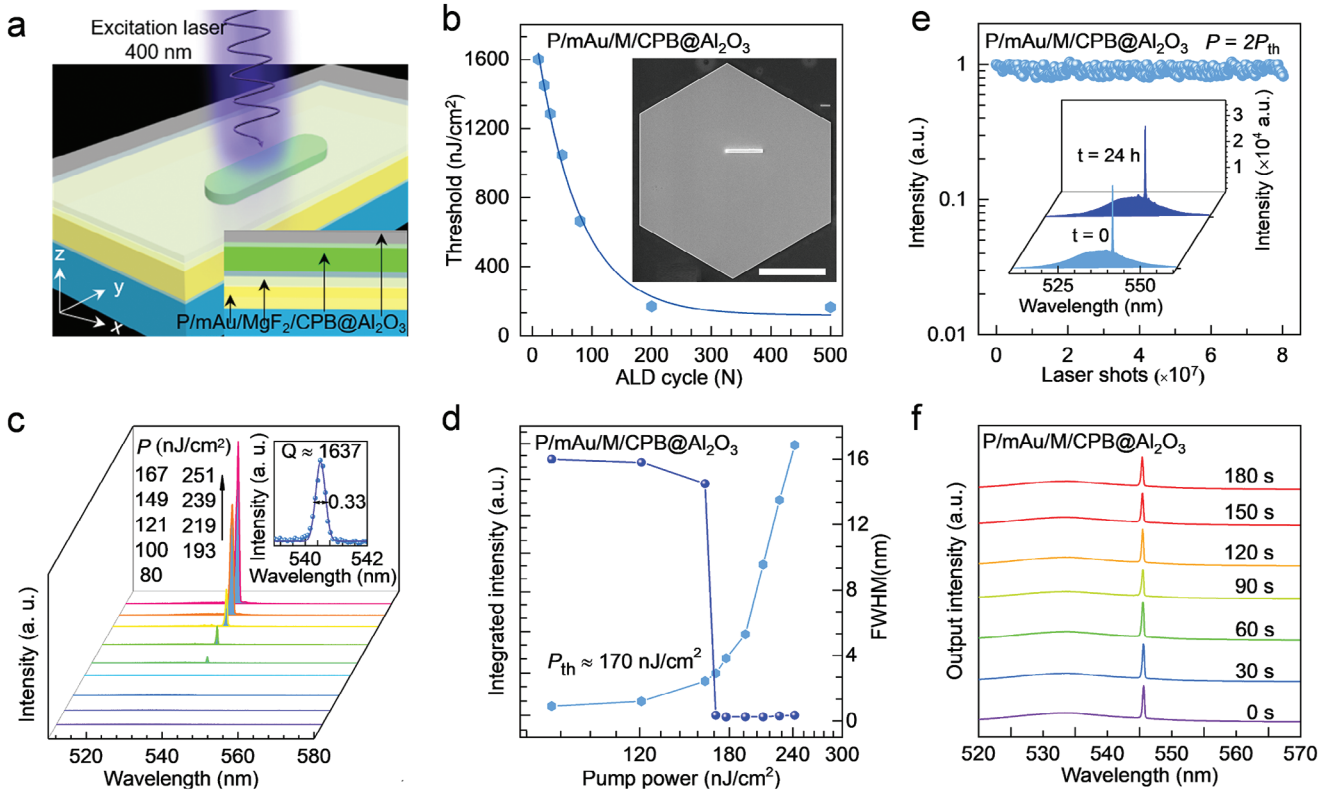

Figure 3. Lasing characteristics of P/mAu/M/CPB@Al_2O_3 plasmon nanolasers. a) Schematic of P/mAu/M/CPB@Al_2O_3 plasmon device. The beam of femtosecond pulsed laser (400 nm, 100 fs, 1KHz) is used to pump the whole $CsPbBr_3$ nanorod. b) The lasing threshold of P/mAu/M/CPB@Al_2O_3 plasmon nanolasers as a function of ALD cycles. Inset: SEM image of the plasmonic device with Al_2O_3 modification (≈200 ALD cycles). Scale bar: 10 μm. c) Pump power-dependent emission spectra of the P/mAu/M/CPB@Al_2O_3 device with P increasing from 80 to 251 nJ cm^{-2}. Inset: the magnified view of a lasing threshold mode fitted by the Lorentzian function. d) Integrated the total emission intensity (sky blue hexagon), and mode linewidth (blue ball) as a function of pump power show a threshold behavior at P_{th} ≈ 170 nJ cm^{-2}. e) Normalized lasing intensities of the P/mAu/M/CPB@Al_2O_3 device as a function of excitation pulse number under continuous operation of 24 h (295 K and 30% relative humidity). Inset: the lasing spectra of the P/mAu/M/CPB@Al_2O_3 device under start (t = 0) and after 24 h, respectively. f) Lasing spectra of the P/mAu/M/CPB@Al_2O_3 device collected from 0 to 180 s after being immersed in DMF.

levels off, thus indicating formation of the dense alumina film on the whole surface of $CsPbBr_3$ nanorods (Figure 2d). The PL intensity after 200 ALD cycles is increased more than nine times than bare $CsPbBr_3$ nanorods (Figure 2d inset), and the PL lifetime is decreased ≈3 times (Figure S8, Supporting Information). Apparently, the enhancement of PL intensity is mainly induced by a faster radiative recombination, which may originate from the passivation effect of Pb–O–Al bond to decrease nonradiative states.[26] In addition, the previous report reveals that the enhancement of radiative rate is ascribed to a high localized electronic state density and a larger exciton binding energy, which are induced by oxide-bonded surface states (Pb–O–Al bond).[26] Because the lower dielectric constants of Al_2O_3 increase the Coulomb interaction of electron-hole pairs. For further revealing of the CPB@Al_2O_3 sample surface radiative states, we carried out the PL spectra with different excitation powers (P varying from 1.56 to 37.56 μW) to investigate the excited-state dynamics (Figure 2e). The integrated PL intensity (I_{PL}) serves as the excitation density power-law function, $I_{PL} \propto P^k$,[43] with a power-law exponent of 0.95 for CPB@Al_2O_3 samples (hexagon in Figure 2e). Where the power-law exponent k = 1 and k = 2 denotes free carrier and excitons recombination processes, respectively.[43,44] The value of 1.46 for $CsPbBr_3$ nanorod sample (dot in Figure 2e) indicates the coexistence of monomolecular (excitons) and bimolecular (free carriers). Therefore, CPB@Al_2O_3 samples have a higher exciton recombination ratio due to the smaller k value, which further identifies a larger exciton binding energy of that.[27] These research results promise to lower the lasing threshold and enhance the sensitivity of the strain-gauge sensor.

The construction of Al_2O_3-modified nanolaser schematically illustrated in **Figure 3a**, which consists of a $CsPbBr_3$ nanorod (T ≈ 130 nm, W ≈ 200 nm, L ≈ 8 μm, Figure 3b inset) sitting on the monocrystal Au surface separated by MgF_2 (T ≈ 5 nm) insulating gap layer, and then coating ≈20 nm-thick Al_2O_3 as encapsulation layer. SEM image shows that the device P/mAu/M/CPB@Al_2O_3 has a smoothed surface morphology after Al_2O_3 modification (Figure 3b inset). Using femtosecond pulsed laser (400 nm, 100 fs, 1 kHz), we further investigated the P_{th} in these devices (P/mAu/M/CPB@Al_2O_3) with increasing the ALD cycles. When we increased the ALD cycles, the P_{th} of P/mAu/M/CPB@Al_2O_3 device reduced rapidly from 1600 nJ cm^{-2} (10 ALD cycles) to 170 nJ cm^{-2} (200 ALD cycles) and then leveling off (Figure 3b), thereby lowering the P_{th} ≈16 times compared with the P/mAu/M/CPB devices

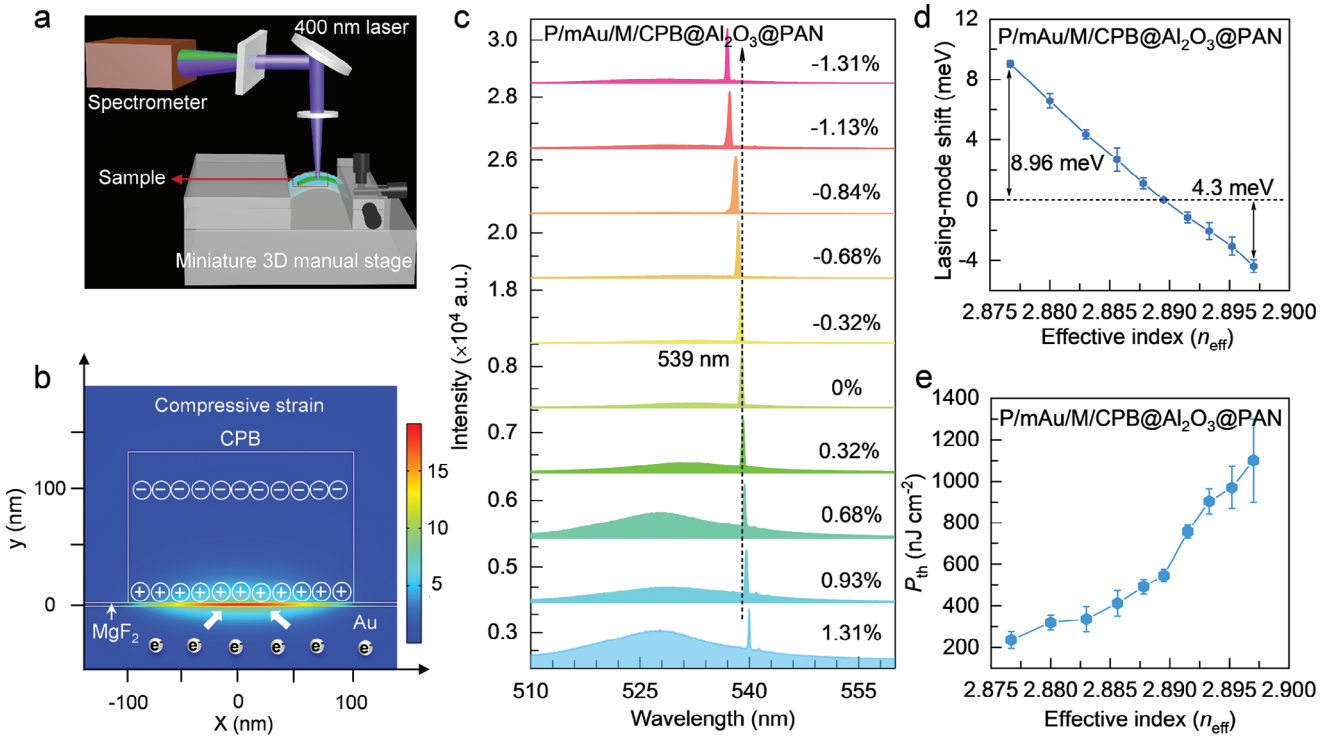

Figure 4. Mechanically robust strain-gauge nanolaser. a) Schematic illustration of the lasing spectra measurement for P/mAu/M/CPB@Al_2O_3@PAN device under uniaxial tensile strain. b) Calculated electric field (|E|) profiles of $CsPbBr_3$ nanorod on monocrystal Au at a wavelength of 540 nm. The thickness and width of the $CsPbBr_3$ nanorod are ≈130 and ≈200 nm, respectively. Because of the piezoelectric polarization effect of the $CsPbBr_3$ nanorods, the piezoelectric polarization charges formed in the $CsPbBr_3$ nanorods under compressive strain, leading to more electrons accumulating at the interface of monocrystal Au and $CsPbBr_3$ nanorods. c) Lasing spectra of P/mAu/M/CPB@Al_2O_3@PAN device under different degrees of compressive strain from $\epsilon = 0\%$ to $\epsilon = -1.31\%$ as $P = 1000$ nJ cm^{-2}. d) Lasing-mode shift (ΔE) and e) lasing threshold (P_{th}) obtained from (c) as a function of effective index (n_{eff}) for the P/mAu/M/CPB@Al_2O_3@PAN device, uncertainties of ΔE and P_{th}, indicated by the error bars.

(Figure S9, Supporting Information). The decrease of P_{th} corresponds well to enhancement of the PL intensity, which elucidates the passivation effect of Pb–O–Al bond to increase the radiative recombination.[26] The power dependent emission spectra of a P/mAu/M/CPB@Al_2O_3 device was further systematic studied under femtosecond laser excitation (400 nm, 100 fs, 1 kHz), as shown in Figure 3c. At a low pump fluence ($P < 167$ nJ cm^{-2}), the spectral was dominated by spontaneous emission (SE) centered at 531 nm with a full width at half maximum (FWHM) of ≈16 nm. After above threshold ($P > 167$ nJ cm^{-2}), a single-mode lasing emerged at 540 nm and the FWHM jumps from 16 nm down to ≈0.33 nm (Figure 3d, blue ball), unveiling a significant increase of temporal coherence. Besides, the relative lasing intensity (I) achieved superlinearly increase, eventually completely dominating the emission spectrum. The nonlinear response of the PL output intensity as a function of P confirms the emergence of lasing oscillation, from which the P_{th} was derived to be ≈170 nJ cm^{-2} (Figure 3d, sky blue hexagon), ensuring a high-quality cavity mode. The Q-factor is calculated to be 1637 according to dividing the mode wavelength ($\lambda = 540$ nm) by the mode linewidth ($\delta\lambda \approx 0.33$ nm, Figure 3c inset), which indicates that the passivation effect of Pb–O–Al bond effectively improved the cavity mode quality of P/mAu/M/CPB@Al_2O_3 device compared with P/mAu/M/CPB device (Figure S9a–c, Supporting Information).

We also further investigate the optical stability of P/mAu/M/CPB@Al_2O_3 device at ambient conditions (24 °C and 30% relative humidity). After ALD coating ≈20 nm-thick Al_2O_3 layer, the lasing spectra are collected every five minutes under continuous pulsed laser excitation (400 nm, 100 fs, 1 kHz) for 24 h. Figure 3e shows the lasing output intensity of P/mAu/M/CPB@Al_2O_3 device under 350 nJ cm^{-2} (≈2 P_{th}) pumping as a function of laser pulse, after 8 × 108 laser pulses without obvious dropping (Figure 3e inset), thus exhibiting excellent optical stability. In addition, Al_2O_3-modified the P/mAu/M/CPB@Al_2O_3 device can well protected $CsPbBr_3$ nanorods against polar solvents[35,36] (such as H_2O or N,N-Dimethylformamide (DMF)). Stable lasing behavior is observed after 180 s immersion in DMF, confirming the enhancement of material's stability after Al_2O_3-modification (Figure 3f). Therefore, we can spin-coating ≈30 nm-thick PAN (10 mg mL^{-1} in DMF, Note S1, Supporting Information) on the surface of P/mAu/M/CPB@Al_2O_3 device to fix the $CsPbBr_3$ nanorods, which will well realize the visual response of tensile and compressive strain in our strain-gauge nanolasers.

To characterize the sensing property of our strain-gauge sensor (P/mAu/M/CPB@Al_2O_3@PAN), we used a miniature 3D manual moving stage to apply the bend stress on the device (**Figure 4a**). The construction of our strain-guage sensor and physical photograph of the measurement setup are illustrated in

Figure S10a,b (Supporting Information), respectively. The electric field |E| profiles of $CsPbBr_3$ nanorod ($\lambda \approx 540$ nm) elucidates the basic working principle of the stress responsive plasmonic nanolasers[17,21,45] (Figure 4b). When applying strain on $CsPbBr_3$ nanorod by bending the PEN substrate, the piezoelectric charges were generated on $CsPbBr_3$ nanorod because of the piezoelectric polarization effect, which can alter the electron density (N_c) of the monocrystal Au surface.[17,20,21] When a compressive strain is applied, the lower surface of $CsPbBr_3$ nanorod is stretched to generate the positive piezoelectric charges, and more electrons accumulate at the single-crystal Au surface (Figure 4b), causing an increase in the plasmon resonant frequency to reduce the radiative loss,[17,21,45] which has been validated in our previous work. In contrast, the N_c and plasmon resonant frequency at the single-crystal Au surface should reduce under applying tensile strain[45] (Figure S11a,b, Supporting Information). Therefore, we utilized the Drude–Lorentz model to describe the optical properties of single-crystal Au with variation of strain (ϵ from 1.31 to −1.31%).[46–48] Here, the plasma frequency (ω_p) of single-crystal Au can be written as following:

$$\omega_p = \sqrt{N_c e^2 / m_e \varepsilon_0} \tag{1}$$

where m_e and ϵ_0 are effective electron mass and vacuum dielectric constant, respectively. The dielectric function of single-crystal Au ($\hat{\varepsilon}_r(\omega)$) can be expressed in the following form:

$$\hat{\varepsilon}_r(\omega) = 1 - \frac{\Omega_p^2}{\omega\left(\omega - i\Gamma_0\right)} + \sum_{j=1}^{k} \frac{f_j \omega_p^2}{\left(\omega_j^2 - \omega^2\right) + i\omega\Gamma_j} \tag{2}$$

where k is the number of oscillators with frequency ω_j, strength f_j, and lifetime $1/\Gamma_j$.[46–48] As a result, when changes the N_c (5.5×10^{22} cm^{-3} – 6.0×10^{22} cm^{-3}) of single-crystal Au surface, it will affect the dielectric function (ϵ) of single-crystal Au (Figure S12a–c, Supporting Information), eventually influencing that of the propagation distance L_m (Figure S12d, Supporting Information) and effective refractive index (n_{eff}, Figure S12e,f, Supporting Information). According to the Maxwell's equations, we ultimately obtained the effective index (n_{eff} = 2.8767–2.8970) of our strain-gauge sensor (P/mAu/M/CPB@Al_2O_3@PAN) with changing N_c from 5.5×10^{22} cm^{-3} to 6.0×10^{22} cm^{-3}. This result reveals that a minor alteration in N_c induces surface plasmon polariton (SPP) and laser characteristic changes (such as λ, I, and P_{th}),[8,13,21,31] which provide a reliable for sensing application based on P/mAu/M/CPB@Al_2O_3@PAN device.

As shown in Figure 4c, we observed a monotonic linear blueshift of the laser peak from 539 nm to 537 nm (≈8.96 meV) when gradually applied the compressive strains from ϵ = 0% up to ϵ = −1.31%, however, ≈1 nm redshift (≈4.3 meV) of the lasing wavelength was achieved with varying tensile strain from ϵ = 0% to ϵ = 1.31%. The repeated experimental results reveal that our strain-gauge sensors (P/mAu/M/CPB@Al_2O_3@PAN) have a reliable sensing behavior (Figure 4d). In addition, the lasing intensity also changes with n_{eff}, which increased ≈70% with applying compressive strain ϵ from 0% to −1.31%, while reduced ≈50% with changing tensile strain ϵ from 0% to 1.31% (Figure S13, Supporting Information). Compared with lasing intensity, the threshold was monotonic decreased from 600 nJ cm^{-2} (ϵ = 0%, n_{eff} = 2.8895) to 210 nJ cm^{-2} (ϵ = −1.31%, n_{eff} = 2.8767), with the performance of ≈60% enhancement (Figure 4e). Conversely, the P_{th} increased ≈45% with applying tensile strain up to ϵ = 1.31%, the corresponding n_{eff} rised to 2.8936 and P_{th} was as high as 1100 nJ cm^{-2} (Figure 4e). It is worth noting that the sensing behavior was also confirmed to be reliable through repeated measurements (Figure 4e). More importantly, these strain-responsive single-mode lasing peaks with a FWHM <0.4 nm not only avoid modal competition but also lay the foundation for high-resolution sensing application.[8]

To assess the sensing performance of the strain-gauge nanolaser, three key parameters, such as sensitivity (in short, S), figure of merit (in short, FOM), and optical strain-resolving factor (in short, F_{OSR}) were employed.[31,49] The sensitivity of a sensor is defined as $S_\lambda = \lambda_\epsilon - \lambda_0/\Delta n$, $S_I = I_\epsilon - I_0/\Delta n$, or $S_{P_{th}} = P_{th(\epsilon)} - P_{th(0)}/\Delta n$.[31,49] In **Figure 5a**, the wavelength sensitivity (S_λ) was plotted as a function of n_{eff} of our strain-gauge sensor, which yield sensitivities of ≈160 nm RIU^{-1} under compressive strain (ϵ = −1.31%) and ~130 nm RIU^{-1} under tensile strain (ϵ = 1.31%). Similarly, the highest S_I and $S_{P_{th}}$ was estimated 4.6 × 10^6 RIU^{-1} and 1.9 × 10^5 nJ cm^{-2} RIU^{-1}, respectively (Figure S14a,b, Supporting Information). To compare these parameters between different kinds of sensing device, we further used FOM which considers the sharpness of the resonance and is an important dimensionless quantity (for details see Note S3, Supporting Information).[50,51] The FOM_λ of the wavelength sensing can be calculated according to $FOM_\lambda = \frac{\Delta\lambda/\Delta n}{\delta\lambda}$, which acquired to be ≈600 ± 50 RIU^{-1} to 500 ± 50 RIU^{-1} under strain ranging from ϵ = −1.31% to ϵ = 1.31% (Figure 5b). Therefore, it can be comparable with the plasmonic guided-mode resonances (GMRs),[52] whereas it is far more than hybrid plasmonic structure.[49,53] In addition, the optical stress-resolving factor (F_{OSR}) can be defined as $\Delta\lambda/\epsilon/\delta\lambda$, which were estimated in the range of 400 ± 200 as a function of the external mechanical strain[8] (Figure 5c). Consequently, a minimum strain of 0.3% is spectrally resolvable in our strain-gauge nanolaser. We further investigate the stability of the strain-gauge nanolaser, the S_λ barely alters after bending 25 cycles for compressive and tensile strain, exhibiting the repeatability and stability (Figure 5d). However, owing to the brittleness and poor mechanical compatibility of perovskite monocrystal material,[54] and further improvements in the bending stability of our sensor are needed.

3. Conclusion

In summary, this work has demonstrated an ultrasensitive strain-gauge nanolaser (P/mAu/M/CPB@Al_2O_3@PAN) based on piezoelectric-effect, with the merits of high resolution, non-contact interaction, and simple construction. Al_2O_3-modified $CsPbBr_3$ nanorods exhibited a single-mode laser with P_{th} dramatically reducing to ≈170 nJ cm^{-2} as well as the high Q-factor (1637). Mechanical control of bending strain induces the change in the piezoelectricity-induced n_{eff}, which allows the manipulation of the photonic band gap in P/mAu/M/CPB@Al_2O_3@PAN device, and the subsequent shift of low-loss single-mode lasing serves as signal sources with high recognizability (F_{OSR} ≈ 600), ultrasensitivity (S_λ ≈ 160 nm RIU^{-1}), and superior mechanical reliability for sensing application of a strain-gauge nanolaser. Our

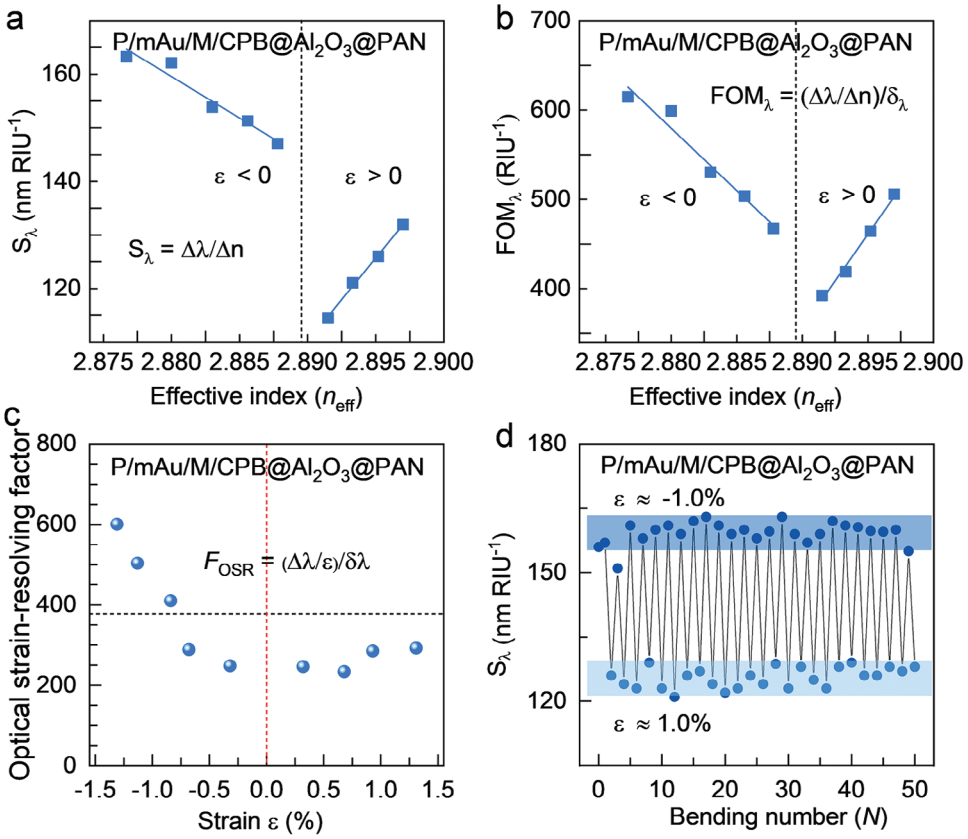

Figure 5. The sensing performance of the strain-gauge nanolaser. a) The sensitivity S_λ and b) FOM_λ of the wavelength sensing are plotted as a function of effective index (n_{eff}) for the P/mAu/M/CPB@Al_2O_3@PAN device with applying strain. The black dotted lines in (a) and (b) are the situation of without strain (ϵ). c) The calculated F_{OSR} as a function of the applied strain (ϵ). The red and black dotted lines are the experimental singularity line ($\epsilon = 0\%$) and the mean F_{OSR}, respectively. d) Cycle stability tests of the S_λ change from $\epsilon = 1.0\%$ and $\epsilon = -1.0\%$.

strategy can be used to develop novel color-perceived sensing nanodevices to perceive the local surface strain in many structures, and these results might establish the foundation for promoting the development of flexible photonic devices as a module of artificial smart-skins.

Supporting Information

Supporting Information is available from the Wiley Online Library or from the author.

Acknowledgements

M.L. and J.L. contributed equally to this work. C.P. and M.L. conceived the idea. C.P., M.L., and J.L. designed the experiments and wrote the manuscript. M.L. prepared the samples and performed all the spectroscopy measurements. All authors discussed the results and commented on the manuscript. C.P. acknowledge the funding support from National Natural Science Foundation of China (Nos. 62105035, 52125205, 52250398, U20A20166, 52192614, and 52003101), National Key R&D Program of China (Nos. 2021YFB3200302 and 2021YFB3200304), Natural Science Foundation of Beijing Municipality (Nos. Z180011 and 2222088), Shenzhen Science and Technology Program (No. KQTD20170810105439418) and the Fundamental Research Funds for the Central Universities. The Natural Science Foundation of Jiangsu Province (No. BK20231441).

Conflict of Interest

The authors declare no conflict of interest.

Data Availability Statement

The data that support the findings of this study are available from the corresponding author upon reasonable request.

Keywords

$CsPbBr_3$ nanorods, piezoelectric effect, single-mode lasing, strain-gauge sensor, ultrasensitive

Received: March 3, 2024
Revised: April 20, 2024
Published online:

[1] X. G. Yu, Z. Q. Xie, Y. Yu, J. Y. Lee, A. Vazquez-Guardado, H. W. Luan, J. Ruban, X. Ning, A. Akhtar, D. F. Li, B. W. Ji, Y. M. Liu, R. J. Sun, J. Y. Cao, Q. Z. Huo, Y. S. Zhong, C. M. Lee, S. Y. Kim, P. Gutruf, C. X. Zhang, Y. G. Xue, Q. L. Guo, A. Chempakasseril, P. L. Tian, W. Lu, J. Y. Jeong, Y. J. Yu, J. Cornman, C. Tan, B. H. Kim, et al., *Nature* **2019**, *575*, 473.

[2] A. Chortos, J. Liu, Z. N. Bao, *Nat. Mater.* **2016**, *15*, 937.
[3] C. X. Wei, L. B. Bai, X. An, M. Xu, W. Liu, W. Z. Zhang, M. Singh, K. Shen, Y. M. Han, L. L. Sun, J. Y. Lin, Q. Zhao, Y. J. Zhang, Y. G. Yang, M. N. Yu, Y. X. Li, N. Sun, Y. F. Han, L. H. Xie, C. J. Ou, B. Sun, X. H. Ding, C. X. Xu, Z. F. An, R. F. Chen, H. F. Ling, W. Li, J. P. Wang, W. Huang, *Chem* **2022**, *8*, 1427.
[4] C. F. Pan, L. Dong, G. Zhu, S. M. Niu, R. M. Yu, Q. Yang, Y. Liu, Z. L. Wang, *Nat. Photonics* **2013**, *7*, 752.
[5] T. Y. Yokota, P. Zalar, M. Kaltenbrunner, H. Jinno, N. J. Matsuhisa, H. K. Kitanosako, Y. Tanchibana, W. Yukita, M. Koizumi, T. Someya, *Sci. Adv.* **2016**, *2*, 1501856.
[6] R. R. Bao, J. Tao, C. F. Pan, Z. L. Wang, *Small Sci.* **2021**, *1*, 2000060.
[7] C. H. Zhang, H. Y. Dong, C. Zhang, Y. Q. Fan, J. N. Yao, Y. S. Zhao, *Sci. Adv.* **2021**, *7*, eabh3530.
[8] J.-H. Choi, Y.-S. No, J.-P. So, J. M. Lee, K.-H. Kim, M.-S. Hwang, S.-H. Kwon, H.-G. Park, *Nat. Commun.* **2016**, *7*, 11569.
[9] L. Zhang, J. Pan, Z. Zhang, H. Wu, N. Yao, D. W. Cai, Y. X. Xu, J. Zhang, G. F. Sun, L. Q. Wang, W. D. Geng, W. G. Jin, W. Fang, D. W. Di, L. M. Tong, *Opto-Electron. Adv.* **2020**, *3*, 190022.
[10] M. Karl, J. M. E. Glackin, M. Schubert, N. M. Kronenberg, G. A. Turnbull, I. D. W. Samuel, M. C. Gather, *Nat. Commun.* **2018**, *9*, 1525.
[11] H. C. Zhao, K. O'Brien, S. Li, R. F. Shepherd, *Sci. Robot.* **2016**, *1*, eaai7529.
[12] H. K. Jinno, T. Y. Yokota, M. Koizumi, W. Yukita, M. Saito, I. Osaka, K. Fukuda, T. Someya, *Nat. Commun.* **2021**, *12*, 2234.
[13] D. Q. Wang, M. R. Bourgeois, W.-K. Lee, R. Li, D. Trivedi, M. P. Knudson, W. J. Wang, G. C. Schatz, T. W. Odom, *Nano Lett.* **2018**, *18*, 4549.
[14] X. T. Gan, H. N. Clevenson, D. Englund, *ACS Photonics* **2017**, *4*, 1591.
[15] T.-W. Lu, C.-C. Wu, P.-T. Lee, *ACS Photonics* **2018**, *5*, 2767.
[16] C. L. Yu, H. W. Kim, N. D. Leon, I. W. Frank, J. T. Robinson, M. McCutcheon, M. Z. Liu, M. D. Lukin, M. Loncar, H. K. Park, *Nano Lett.* **2013**, *13*, 248.
[17] C. F. Pan, J. Y. Zhai, Z. L. Wang, *Chem. Rev.* **2019**, *119*, 9303.
[18] Y. Y. Peng, J. F. Lu, D. F. Peng, W. D. Ma, F. T. Li, Q. S. Chen, X. D. Wang, J. L. Sun, H. T. Liu, C. F. Pan, *Adv. Funct. Mater.* **2019**, *29*, 1905051.
[19] S. D. Cheng, S. C. Han, Z. Y. Cao, C. C. Xu, X. S. Fang, X. Y. Wang, *Small* **2020**, *16*, 1907461.
[20] Z. Yang, J. F. Lu, M. H. Zhuge, Y. Cheng, J. F. Hu, F. T. Li, S. Qiao, Y. F. Zhang, G. F. Hu, Q. Yang, D. F. Peng, K. H. Liu, C. f. Pan, *Adv. Mater.* **2019**, *31*, 1900647.
[21] M. L. Li, J. F. Lu, P. Wan, M. M. Jiang, F. Lin, X. X. Wu, X. F. Liu, C. F. Pan, *Adv. Opt. Mater.* **2023**, *11*, 2202723.
[22] X. H. Cao, S. Y. Xing, R. C. Lai, Y. X. Lian, Y. X. Wang, J. Y. Xu, C. Zou, B. D. Zhao, D. W. Di, *Adv. Funct. Mater.* **2023**, *33*, 2211841.
[23] H. J. Tang, Y. H. Wang, Y. M. Chen, K. Y. Wang, X. X. He, C. Huang, S. M. Xiao, S. H. Yu, Q. H. Song, *Nano Lett.* **2023**, *23*, 3418.
[24] S. Yang, W. Bao, X. Z. Liu, J. M. Kim, R. K. Zhao, R. M. Ma, Y. Wang, X. Zhang, *Matter* **2021**, *4*, 4042.
[25] D. B. Kim, J. W. Lee, Y. S. Cho, *Adv. Funct. Mater.* **2021**, *31*, 2007131.
[26] M. Z. Peng, Z. Li, C. H. Liu, Q. Zheng, X. Q. Shi, M. Song, Y. Zhang, S. Y. Du, J. Y. Zhai, Z. L. Wang, *ACS Nano* **2015**, *9*, 3143.
[27] H. Y. Dong, C. H. Zhang, W. J. Nie, S. K. Duan, C. N. Saggau, M. Tang, M. S. Zhu, Y. S. Zhao, L. B. Ma, O. G. Schmidt, *Angew. Chem., Int. Ed.* **2022**, *61*, 202115875.
[28] Y. N. Jiao, S. H. Yi, H. W. Wang, B. Li, W. Z. Hao, L. L. Pan, Y. Shi, X. Y. Li, P. F. Liu, H. Zhang, C. F. Gao, J. J. Zhao, J. Lu, *Adv. Funct. Mater.* **2020**, *31*, 2006243.
[29] G. Dai, L. Wang, S. J. Cheng, Y. Chen, X. Liu, L. G. Deng, H. Z. Zhong, *ACS Photonics* **2020**, *7*, 2390.
[30] R.-M. Ma, S. Ota, Y. M. Li, S. Yang, X. Zhang, *Nat. Nanotech.* **2014**, *9*, 600.
[31] C. H. Lee, B. J. Lawrie, R. Pooser, K.-G. Lee, C. Rockstuhl, M. Tame, *Chem. Rev.* **2021**, *121*, 4743.
[32] F. Zheng, Z. Chen, J. F. Li, R. Wu, B. Zhang, G. H. Nie, Z. J. Xie, H. Zhang, *Adv. Sci.* **2022**, *9*, 2105231.
[33] T. Y. Xue, W. Y. Liang, Y. W. Li, Y. H. Sun, Y. J. Xiang, Y. P. Zhang, Z. G. Dai, Y. H. Duo, L. M. Wu, K. Qi, B. N. Shivananju, L. J. Zhang, X. Q. Cui, H. Zhang, Q. L. Bao, *Nat. Commun.* **2019**, *10*, 28.
[34] Z. Chen, J. F. Li, T. Z. Li, T. J. Fan, C. L. Meng, C. Z. Li, J. L. Kang, L. X. Chai, Y. B. Hao, Y. X. Tang, O. A. Al-hartomy, S. Wageh, A. G. Al-Sehemi, Z. G. Luo, J. T. Yu, Y. H. Shao, D. F. Li, S. Feng, W. J. Liu, Y. Q. He, X. P. Ma, Z. J. Xie, H. Zhang, *Natl. Sci. Rev.* **2022**, *9*, Nwac104.
[35] R. X. Li, B. B. Li, X. Fang, D. K. Wang, Y. Q. Shi, X. Liu, R. Chen, Z. P. Wei, *Adv. Mater.* **2021**, *33*, 2100466.
[36] H. R. Yu, X. L. Xu, H. Liu, Y. Wan, X. Cheng, J. J. Chen, Y. Ye, L. Dai, *ACS Nano* **2020**, *14*, 552.
[37] Q. Y. Xiang, B. Z. Zhou, K. Cao, Y. W. Wen, Y. Li, Z. J. Wang, C. C. Jiang, B. Shan, R. Chen, *Chem. Mater.* **2018**, *30*, 8486.
[38] Q. A. Akkerman, G. Rainó, M. V. Kovalenko, L. Manna, *Nat. Mater.* **2018**, *17*, 394.
[39] L. Xu, S. Yuan, H. Zeng, J. Song, *Mater. Today Nano* **2019**, *6*, 100036.
[40] C. Sun, Z. H. Wu, H.-L. Yip, H. Zhang, X.-F. Jiang, Q. F. Xue, Z. C. Hu, Z. H. Hu, Y. Shen, M. K. Wang, F. Huang, Y. Cao, *Adv. Energy Mater.* **2016**, *6*, 1501534.
[41] S. M. George, *Chem. Rev.* **2010**, *110*, 111.
[42] S. W. Eaton, M. L. Lai, N. A. Gibson, A. B. Wong, L. T. Dou, J. Ma, L.-W. Wang, S. R. Leone, P. D. Yang, *Proc. Natl. Acad. Sci. USA* **2016**, *113*, 1993.
[43] H. P. He, Q. Q. Yu, H. Li, J. Li, J. J. Si, Y. Z. Jin, N. N. Wang, J. P. Wang, J. W. He, X. K. Wang, Y. Zhang, Z. Z. Ye, *Nat. Commun.* **2016**, *7*, 10896.
[44] N. Droseros, G. L. Longo, J. C. Brauer, M. Sessolo, H. J. Bolink, N. Banerji, *ACS Energy Lett.* **2018**, *3*, 1458.
[45] H. Li, J.-H. Li, K.-B. Hong, M.-W. Yu, Y.-C. Chung, C.-Y. Hsu, J.-H. Yang, C.-W. Cheng, Z.-T. Huang, K.-P. Chen, T.-R. Lin, S. Gwo, T.-C. Lu, *Nano Lett.* **2019**, *19*, 5017.
[46] L.-Y. Chen, D. W. Lynch, *Phys. Rev. B* **1987**, *36*, 1425.
[47] S. J. Youn, T. H. Rho, B. I. Min, K. S. Kim, *Phys. Stat. Sol.* **2007**, *244*, 1354.
[48] S. Link, M. A. Ei-Sayed, *J. Phys. Chem. B* **1999**, *103*, 8410.
[49] S. Wang, B. Li, X.-Y. Wang, H.-Z. Chen, Y.-L. Wang, X.-W. Zhang, L. Dai, R.-M. Ma, *ACS Photonics* **2017**, *4*, 1355.
[50] Y. Xu, P. Bai, X. D. Zhou, Y. Akimov, C. E. Png, L.-K. Ang, W. Knoll, L. Wu, *Adv. Opt. Mater.* **2019**, *7*, 1801433.
[51] B. Q. Wang, P. Yu, W. H. Wang, X. T. Zhang, H.-C. Kuo, H. X. Xu, Z. M. Wang, *Adv. Opt. Mater.* **2021**, *9*, 2001520.
[52] Z. Q. Liu, G. Q. Liu, X. S. Liu, G. L. Fu, *Nanotechnology* **2020**, *31*, 115208.
[53] X. Y. Wang, Y. L. Wang, S. Wang, B. Li, X. W. Zhang, L. Dai, R. M. Ma, *Nanophotonics* **2017**, *6*, 472.
[54] A. Liu, I. Mukhin, R. M. Islamova, J. J. Tian, *Adv. Funct. Mater.* **2023**, *34*, 2312209.